

1 **Fully Automated Detection of Paramagnetic Rims in Multiple Sclerosis Lesions on 3T**  
2 **Susceptibility-Based MR Imaging**

3

4 **Carolyn Lou MS<sup>1</sup>, Pascal Sati PhD<sup>2,3</sup>, Martina Absinta MD, PhD<sup>2,4</sup>, Kelly Clark MS<sup>1</sup>, Jordan D.**  
5 **Dworkin PhD<sup>5,6</sup>, Alessandra M. Valcarcel PhD<sup>1</sup>, Matthew K. Schindler MD, PhD<sup>7</sup>, Daniel S.**  
6 **Reich MD, PhD<sup>2,4</sup>, Elizabeth M. Sweeney PhD<sup>8\*†</sup>, Russell T. Shinohara PhD<sup>1,9\*†</sup>**

7

8 <sup>1</sup>Penn Statistics in Imaging and Visualization Endeavor (PennSIVE) Center, Department of  
9 Biostatistics, Epidemiology, and Informatics, University of Pennsylvania, Philadelphia, PA, USA.

10 <sup>2</sup>Translational Neuroradiology Section, National Institute of Neurological Disorders and Stroke  
11 (NINDS), National Institutes of Health (NIH), Bethesda, Maryland, USA.

12 <sup>3</sup>Department of Neurology, Cedars-Sinai Medical Center, Los Angeles, California, USA.

13 <sup>4</sup>Department of Neurology, Johns Hopkins School of Medicine, Baltimore, Maryland, USA.

14 <sup>5</sup>Department of Psychiatry, Columbia University Medical Center, New York, New York, USA.

15 <sup>6</sup>New York State Psychiatric Institute, New York, New York, USA.

16 <sup>7</sup>Department of Neurology, University of Pennsylvania, Philadelphia, PA, USA.

17 <sup>8</sup>Department of Population Health Sciences, Weill Cornell Medicine, New York, New York, USA.

18 <sup>9</sup>Center for Biomedical Image Computing and Analytics, Department of Radiology, University of  
19 Pennsylvania, Philadelphia, Pennsylvania, USA.

20

21 \*Both authors contributed equally to this work.

22

23 †Corresponding Authors:

24 Email: [ems4003@med.cornell.edu](mailto:ems4003@med.cornell.edu) (EMS)

25 Email: [rshi@pennmedicine.upenn.edu](mailto:rshi@pennmedicine.upenn.edu) (RTS)

26

27 **Abstract**

28

29 **Background and Purpose:** The presence of a paramagnetic rim around a white matter lesion  
30 has recently been shown to be a hallmark of a particular pathological type of multiple sclerosis  
31 (MS) lesion. Increased prevalence of these paramagnetic rim lesions (PRLs) is associated with a  
32 more severe disease course in MS. The identification of these lesions is time-consuming to  
33 perform manually. We present a method to automatically detect PRLs on 3T T2\*-phase images.

34

35 **Methods:** T1-weighted, T2-FLAIR, and T2\*-phase MRI of the brain were collected at 3T for 19  
36 subjects with MS. The images were then processed with lesion segmentation, lesion center  
37 detection, lesion labelling, and lesion-level radiomic feature extraction. A total of 877 lesions  
38 were identified, 118 (13%) of which contained a paramagnetic rim. We divided our data into a  
39 training set (15 patients, 673 lesions) and a testing set (4 patients, 204 lesions). We fit a random  
40 forest classification model on the training set and assessed our ability to classify lesions as PRL  
41 on the test set.

42

43 **Results:** The number of PRLs per subject identified via our automated lesion labelling method  
44 was highly correlated with the gold standard count of PRLs per subject,  $r = 0.91$  (95% CI [0.79,  
45 0.97]). The classification algorithm using radiomic features can classify a lesion as PRL or not  
46 with an area under the curve of 0.80 (95% CI [0.67, 0.86]).

47

48 **Conclusion:** This study develops a fully automated technique for the detection of paramagnetic  
49 rim lesions using standard T1 and FLAIR sequences and a T2\*phase sequence obtained on 3T  
50 MR images.

51

52 **Keywords:** magnetic resonance imaging; multiple sclerosis; chronic active lesions; paramagnetic  
53 rim lesions

54

55 **Highlights:**

- 56       • A fully automated method for both the identification and classification of paramagnetic  
57       rim lesions is proposed.
- 58       • Radiomic features in conjunction with machine learning algorithms can accurately  
59       classify paramagnetic rim lesions.
- 60       • Challenges for classification are largely driven by heterogeneity between lesions,  
61       including equivocal rim signatures and lesion location.

## 62 Introduction

63

64 Multiple sclerosis (MS) is a demyelinating and inflammatory disease of the central nervous  
65 system whose hallmark is lesions in the brain and spinal cord (1). These lesions can be detected  
66 *in vivo* with magnetic resonance imaging (MRI) and are often quantified as total lesion volume  
67 and lesion count, both of which can be used as measures of disease burden and to track disease  
68 progression (2). Imaging biomarkers such as these are commonly used in the clinic and as  
69 surrogate endpoints in clinical trials (3,4). However, other known biological processes of MS are  
70 left uncaptured.

71

72 Chronic active lesions, which are a subset of MS lesions that are more prevalent in patients with  
73 more severe disease (5–7), have imaging and histopathology findings suggestive of ongoing  
74 tissue damage (8–10) and have until recently only been detectable by histopathology. These  
75 lesions have been variously termed chronic active, slowly expanding, or smoldering lesions. At  
76 an estimated prevalence of 10-15% of all MS lesions, this type of lesion is sufficiently common  
77 and deleterious to warrant considerable efforts for biomarker development (6,8,9,11). On T2\*  
78 phase MRI contrast, they are identifiable by curvilinear hypointensity along the edge of the  
79 lesion that corresponds with of iron laden phagocytic cells observed on histopathological  
80 specimens (8,9,12). These lesions have been variously termed chronic active, slowly expanding,  
81 or smoldering lesions. Here, we refer to these lesions as paramagnetic rim lesions (PRLs).

82

83 When first observed on MRI, the rim of a PRL was only visible on scans from ultra-high-field  
84 strength (7T) magnets (13–16). Recently, PRLs have been shown to be identifiable on the more  
85 commonly available high-field strength (3T) MRI scans as well, albeit with lower inter- and intra-  
86 rater reliability (17). This development strengthens their viability as a target on clinical MRI  
87 protocols, particularly because the sequences studied can be acquired with high spatial  
88 resolution in less than 4 minutes (18). Previous studies of the PRLs have noted the geometric  
89 nature of the rim and worked to identify the rim on the quantitative susceptibility mapping  
90 (QSM) contrast as well (19–21).

91

92 Because visually inspecting every MS lesion for the presence of a paramagnetic rim is difficult,  
93 time consuming, and prone to inter- and intra-rater variability, an automated method for  
94 identifying PRLs would improve efficiency and facilitate translation of this imaging biomarker  
95 into larger research studies and clinical practice. One way to identify PRLs is through  
96 quantification of visual patterns that objectively characterize these data, which can be  
97 accomplished through radiomics. Radiomics is an emerging field of research that encompasses  
98 the extraction of quantitative features from biomedical images that may reflect underlying  
99 pathophysiology (22). It has been shown to be a useful tool in the analysis of chest CT scans  
100 (23,24) and MR images (25,26). Studies have shown that radiomic features are often useful  
101 predictors of, or are associated with, known hallmarks of disease, although they have not been  
102 used extensively in the MS literature. Here, we use radiomic features along with a random  
103 forest classification model, which can flexibly model high dimensional data. Our method is fully  
104 automated and uses a T2\*-phase volume with isometric voxels and high spatial resolution that  
105 is acquired in a clinically feasible acquisition time at 3T (18).

106

107

## 108 **Materials and Methods**

109

110 Study population:

111 We studied 19 subjects with MS who were scanned under an institutional review board–  
112 approved natural history protocol at the National Institutes of Health (NIH). Subjects' age at the  
113 time of scanning ranged from 20 to 66 years, with a mean age of 45 years (sd = 12) (Table 1).

114

**Table 1: Demographics of Study Sample**

<b>Demographics</b>	
N	19
Age (mean (SD))	45 (12)
Male (%)	8 (42)
Phenotype (%)	
Primary Progressive MS	3 (16)
Relapsing-Remitting MS	11 (58)
Secondary Progressive MS	5 (26)
Disease duration in years (mean (SD))	14.6 (9.1)
EDSS (median (range))	2.5 (1.0—7.0)
Treatment	
untreated	5 (26)
glatiramer acetate	1 (5)
interferon beta-1a	4 (21)
dimethyl fumarate	6 (32)
fingolimod	1 (5)
natalizumab	1 (5)
rituximab	1 (5)

115

116 Written informed consent was obtained from all participants. Data from this study can be  
117 shared upon reasonable request and completion of a Data Transfer Agreement with the  
118 National Institutes of Health.

119

120 MR Imaging acquisition:

121 All subjects were imaged on a Siemens Magnetom Skyra (Siemens, Erlangen, Germany) 3T  
122 scanner, using a body transmit coil and a 32-channel receive array coil, at the National  
123 Institutes of Health in Bethesda, Maryland. Imaging acquisition included the following  
124 sequences:

- 125 • a whole-brain 3D T2-weighted fluid-attenuated inversion recovery (FLAIR) sequence  
126 (repetition time, TR = 4800 ms; echo time, TE = 354 ms; inversion time, TI = 1800 ms; flip  
127 angle, FA = 120°; acquisition time, TA = 6 minutes 30 seconds; 256 axial slices; 1mm  
128 isometric voxel resolution);
- 129 • a whole-brain 3D T1-weighted magnetization-prepared rapid gradient echo (T1) sequence  
130 (TR = 7.8 ms; TE = 3 ms; FA = 18°; TA = 3 minutes 35 seconds; 256 sagittal slices; 1mm  
131 isometric voxel resolution), and
- 132 • a 3D segmented echo-planar imaging (EPI) sequence with whole-brain coverage providing  
133 T2\* magnitude and phase contrasts (TR = 64 ms; TE = 35 ms; flip angle, FA = 10°; TA = 5  
134 minutes 46 seconds; 251 sagittal slices; 0.65mm isometric voxel resolution).

135 Additional standard MRI sequences, including a postcontrast 3D T1-weighted MPRAGE  
136 sequence for the identification of gadolinium-enhancing lesions, were also acquired.

137

138 Manual paramagnetic rim lesion assessment:

139 Supratentorial non-gadolinium enhancing MS lesions were visually inspected for the presence  
140 of a paramagnetic rim on T2\* magnitude and unwrapped phase images by a neurologist with 14  
141 years of experience in neuroimaging science (5,13,17). As previously described (27), a PRL is  
142 identified when a hypointense signal on phase images is observed surrounding the periphery of  
143 the lesion, while being either hyper- or isointense in its inner portion.

144

145 Image preprocessing:

146 Phase images were unwrapped and filtered as previously described (13). T1, FLAIR, and phase  
147 images were then preprocessed using the *fslr* R package (28), an R wrapper for the FSL software  
148 (29,30). Images were visualized with ITK-SNAP (31). The T2\* magnitude contrast was not used  
149 in this method.

150

151 We first applied the N4 inhomogeneity correction algorithm (32). We then rigidly registered  
152 both the T1 and the FLAIR images to the T2\*-phase image space, resampling to 0.65 mm  
153 isometric resolution and using a mutual information cost function and nearest neighbor

154 interpolation. We used multi-atlas skull stripping (MASS) to identify cerebral tissue in the  
155 images in T1 space (33). In two cases, MASS yielded poorly skull-stripped images based on  
156 visual inspection. For those two cases, we instead used the FSL brain extraction tool for skull-  
157 stripping (29). As a final step, we performed WhiteStripe intensity normalization on the  
158 otherwise preprocessed T1, FLAIR, and phase images (34).

159

160 Lesion labelling:

161 Our lesion labelling method relies on access to maps that represent voxel-wise probabilities of  
162 being a lesion, so we chose the automatic lesion segmentation method MIMoSA both for its  
163 ability to integrate multimodal information and for its ability to provide voxel-level probability  
164 maps (35). Manual lesion segmentation was conducted by a research assistant with 1 year of  
165 experience, who was trained by a board-certified neurologist with extensive expertise in  
166 neuroimmunology and MRI.

167

168 We trained the MIMoSA algorithm (36) with the manual segmentations as a gold standard and  
169 the T1 and FLAIR images as input. We implemented a leave-one-out cross-validation approach,  
170 where data from all but one subject was used to train a MIMoSA model, and that model was  
171 subsequently applied to the remaining subject. This was done for every subject in our cohort.  
172 When parallelized across 8 cores of a CPU of an Intel(R) Xeon(R) E5-2699 v4 @ 2.20GHz  
173 processor in a high-performance computing environment, training a single model on 19  
174 subjects took approximately 6 hours.

175

176 From each k-fold model, we extracted probability maps that contain voxel-wise probabilities of  
177 being a white matter lesion. We then binarized these probability maps into lesion segmentation  
178 maps via a subject-specific estimated optimal threshold that was identified out of a user-  
179 provided range of possible thresholds and then chosen based on amount of overlap with a gold-  
180 standard lesion segmentation as measured by a Sørensen-Dice coefficient (37). Because our  
181 lesion segmentation masks did not always cover the entire area of a lesion, we then dilated the



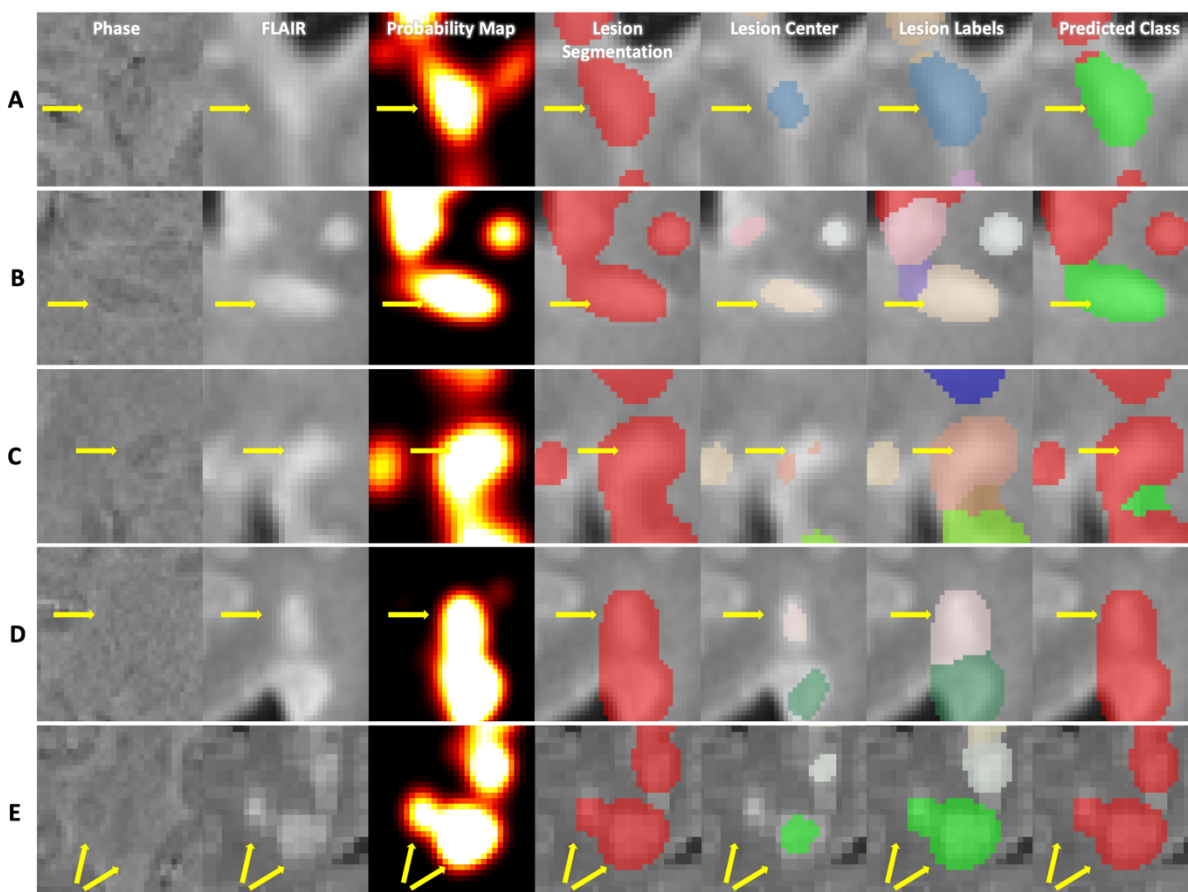
182 masks by one voxel in each direction to increase the likelihood of detecting the paramagnetic  
183 rim signal, which occurs on the boundary of lesions.

184

185 After lesion segmentation masks were obtained, we used the lesion probability maps as input  
186 to a center detection method (38) to identify distinct lesions based on the texture of the lesion  
187 tissue. We then used a nearest-neighbor approach to classify the remainder of the lesion  
188 segmentation map into those identified lesions (Figure 1). At this point, we assigned PRL status  
189 to the identified lesions based on the presence of any overlap with the manual PRL labels  
190 described previously.

191

192 **Figure 1**



193

194 A visualization of the steps of the method for five different lesions. Each column corresponds to  
195 a different part of the method, and each row corresponds to a different lesion of interest. In the

196 last column, lesions classified as PRLs are visualized as green, and lesions classified as not PRLs  
197 are visualized as red. Subfigure A shows a lesion that was both identified as a PRL and classified  
198 as a PRL, i.e. a true positive. Subfigure B shows a lesion that was identified as not a PRL but  
199 classified as a PRL, i.e. a false positive. Correspondingly, subfigure C shows a false negative  
200 lesion, and subfigure D shows a true negative lesion. Subfigure E shows a lesion that was  
201 automatically labelled as a single lesion but is actually a confluence of lesions.

202

203

204 Due to failures in the lesion labelling process, a subset of abnormalities automatically identified  
205 by our method might, to a manual rater, be considered clusters of confluent lesions. Because  
206 we did not have access to manual segmentations of distinct lesions, we instead relied on a  
207 combination of our lesion labelling method and connected components analysis to label lesions  
208 as confluent. Specifically, if connected components only identified one cluster where our lesion  
209 labelling method identified more than one lesion, we labelled the constituent lesions as  
210 confluent.

211

212 Radiomics image analysis:

213 For lesions that were identified with our automatic pipeline, we conducted a radiomics analysis  
214 to characterize each lesion with intensity-based statistics only on the phase contrast (39,40).

215 These include 44 features that summarize the intensities in an individual lesion with measures  
216 that can be described in 3 general ways: statistics that describe the average and spread of the  
217 intensities, statistics that describe the shape of the distribution of intensities, and statistics that  
218 describe the diversity of intensities (40). For example, features like the mean, defined as

219  $\frac{1}{n} \sum_{i=1}^n x_i$ , and interquartile range, defined as  $abs(x_{75\%} - x_{25\%})$ , are included in the first group,  
220 where  $x_i$  represents intensity value at voxel  $i$ . Features like variance, defined as

221  $\frac{1}{n} \sum_{i=1}^n (x_i - mean(x))^2$ , and skew, defined as  $\frac{\frac{1}{n} \sum_{i=1}^n (x_i - mean(x))^3}{sd(x)^3}$ , are included in the second

222 group, and features like energy, defined as  $\sum_{i=1}^n x_i^2$ , uniformity, defined as  $\sum_{i=1}^n p(x_i)^2$ , and

223 entropy, defined as  $\sum_{i=1}^n -p(x_i) \log_2 p(x_i)$ , are included in the third group. A full list and

224 detailed equations for each of the first-order radiomic features can be found in the  
225 supplemental material of (40).

226

227 Prediction model:

228 The radiomic features were used as candidate predictors in our subsequent prediction  
229 modelling for classification of lesions as either being PRL or not. Class labels for each lesion  
230 were previously assigned during the lesion labelling step. We split our dataset into a training set  
231 and test set by subject, randomly assigning lesions from 15 subjects into the training set and  
232 assigning lesions from the remaining 4 subjects into the test set, approximating an 80/20 split.  
233 Both sets were examined to ensure that at least 100 lesions were present in each group.

234

235 Because PRLs were of a minority class (approximately 13% of the lesions were classified as  
236 being a PRL), we used Synthetic Minority Oversampling TEchnique (SMOTE) to synthetically  
237 balance our data (41). With SMOTE, we oversampled the minority class, the PRLs, by the  
238 reciprocal of the percentage of PRLs present in the dataset, and we did not undersample the  
239 majority class. We then trained a random forest classifier, chosen for its ability to flexibly model  
240 a large number of features, with 10-fold cross-validation using the R package *caret* (42,43). We  
241 summarized performance results using 0.5 as a threshold where applicable. We also derived  
242 empirical confidence intervals for those measurements by randomly reassigning the training  
243 and test set and repeating the above process 1000 times. We assessed variable importance in  
244 the random forest as the percent increase in mean-squared error for a model with the variable  
245 over a model with a permuted version of that variable. We then scaled that measure for  
246 comparability across variables.

247

248

249 Post-hoc analysis:

250 An additional board-certified neurologist (MS) with extensive expertise in neuroimmunology  
251 and MRI, who was not involved in the generation of the manual PRL labels, examined each  
252 misclassified lesion. We rated lesions on a 5-point scale, where 1 indicated definitely not a PRL,  
253 2 indicated probably not a PRL, 3 indicated uncertain, 4 indicated probably a PRL, and 5  
254 indicated definitely a PRL. Some lesions were automatically labelled as one lesion but were  
255 actually a confluence of lesions (Figure 1). We assigned manual ratings to these confluent  
256 clusters based on the presence of at least one PRL. We also assessed the method's performance  
257 only for lesions that were not part of a confluent cluster.

258

259

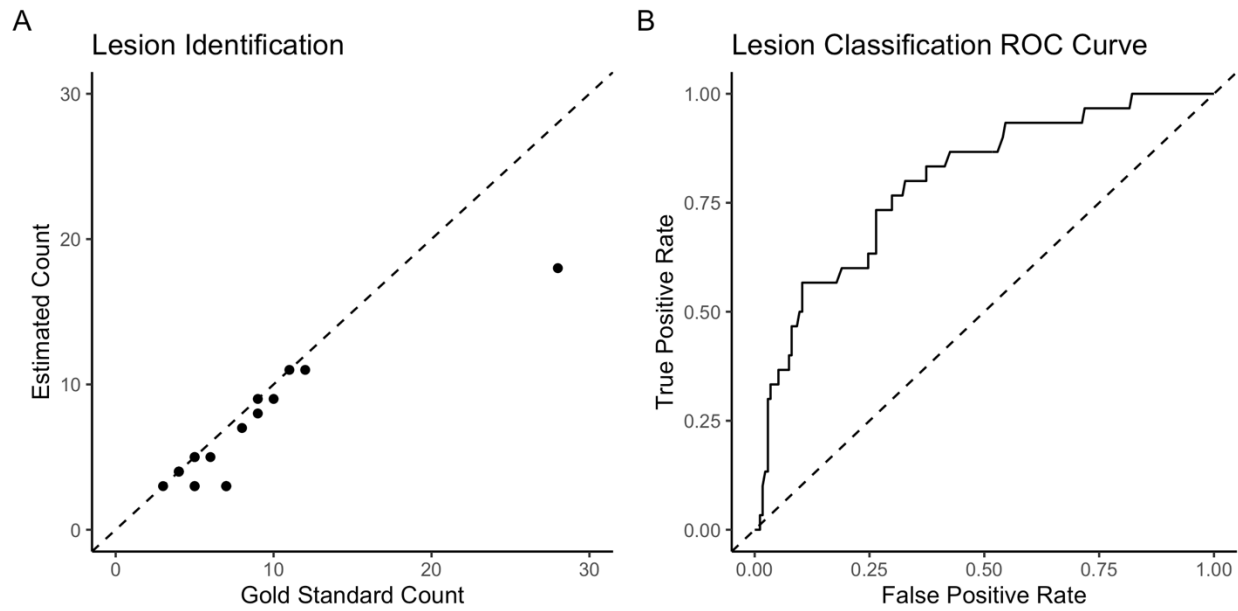
## 260 **Results**

261

262 The final dataset included a total of 877 lesions in 19 subjects identified by our automated  
263 lesion labelling method, 118 (13%) of which we found to be PRLs by overlap with the manual  
264 annotation. The average number of lesions per subject was 46.2 (sd = 19.8), and the average  
265 number of PRLs per subject was 6.2 (sd = 4.0). Table 2 summarizes by subject the total number  
266 of lesions identified from our lesion labelling method, the number of PRLs identified from our  
267 lesion labelling method, and the number of PRLs identified by a manual rater. The number of  
268 identified PRLs by our method was highly correlated with the gold standard count of PRLs,  $r =$   
269 0.91 (95% CI [0.79, 0.97]) (Figure 2).

270

271 **Figure 2**



272

273 Subfigure A shows the gold standard count of PRLs against the number of PRLs identified via

274 our lesion identification method,  $r = 0.91$  (0.79, 0.97). Subfigure B shows the ROC curve after

275 classification,  $AUC = 0.80$  (0.67, 0.86).

276

277 **Table 2: Lesion Counts by Subject**

Subject ID	Automated Total Lesion Count	Automated PRL Count	Manual PRL Count
1	83	9	9
2	35	3	5
3	31	5	6
4	22	3	7
5	40	9	10
6	69	18	28
7	14	3	7
8	54	8	9
9	42	3	7
10	52	11	12
11	27	4	4
12	72	4	4
13	40	3	5
14	28	5	5
15	39	11	11
16	78	4	4
17	36	5	5
18	47	7	8
19	68	3	3

278 The table summarizes the total number of lesions identified per subject, the number of  
279 identified paramagnetic rim lesions (PRL) by our lesion labelling method, and the number of  
280 PRLs identified by a manual rater.

281

282

283 We trained a random forest classification model using PRL status from the lesion labelling  
284 method as the label. In the iteration that we used to derive performance measures, there were  
285 673 lesions in the training set, 88 of which were PRLs, and 204 lesions in the testing set, 30 of  
286 which were PRLs. We were able to classify lesions as PRL or not with an AUC of 0.80 (95% CI  
287 [0.67, 0.86]). Using 0.5 as a probability threshold, 150 lesions were accurately classified as not  
288 PRL, 24 lesions were false positives, 13 were false negatives, and 17 were classified correctly as  
289 PRL (Table 3). A breakdown of the classification results for the test set lesions by subject is also  
290 provided in Table 3, from which we can see that variability in classification accuracy does not  
291 seem to be driven by poor performance in a minority of subjects but rather by heterogeneity in  
292 the lesions themselves.  
293

294 **Table 3: Summary of Classification Performance Measures**

<b>Contingency Table</b>				
	<b>Reference</b>			
<b>Prediction</b>	Rim Negative		Rim Positive	
Rim Negative	150		13	
Rim Positive	24		17	
<b>Performance Measures</b>				
Accuracy	0.82 (0.71, 0.86)			
Positive Predictive Value	0.41 (0.16, 0.53)			
Negative Predictive Value	0.92 (0.87, 0.97)			
False Positive Rate	0.14 (0.08, 0.27)			
False Negative Rate	0.43 (0.22, 0.72)			
Sensitivity	0.57 (0.29, 0.74)			
Specificity	0.86 (0.72, 0.92)			
<b>Testing Set Lesion Classification Count by Subject</b>				
Subject	True Negative	False Negative	False Positive	True Positive
1	70	4	4	5
4	18	2	1	1
11	30	5	11	6
20	32	2	8	5

295 The table summarizes the performance measures we observed for the classification of lesions  
 296 as PRLs or not.

297

298

299 We also examined the results of the method for lesions that were not part of a confluent  
 300 cluster. A total of 62 lesions in the test set were not confluent, and we were able to classify  
 301 them with an AUC of 0.91. Using 0.5 as a probability threshold, 50 lesions were accurately  
 302 classified as not PRL, 4 were false positive, 2 were false negative, and 6 were accurately



303 classified as PRL (Table 4). We provide a summary of additional performance measures in Table  
304 4.

305

306 **Table 4: Summary of Classification Performance Measures, Excluding Confluent Lesions**

<b>Contingency Table</b>		
	<b>Reference</b>	
<b>Prediction</b>	Rim Negative	Rim Positive
Rim Negative	50	4
Rim Positive	2	6

<b>Performance Measures</b>	
Accuracy	0.90
Positive Predictive Value	0.75
Negative Predictive Value	0.92
False Positive Rate	0.04
False Negative Rate	0.40
Sensitivity	0.60
Specificity	0.96

307 The table summarizes the performance measures we observed for the classification of lesions  
308 after exclusion of lesions in confluent clusters.

309

310

311 A visualization of lesions that were true positive, false positive, false negative, and true negative  
312 respectively is provided in Figure 1. From subfigure B, where we see the method illustrated for  
313 a lesion that was identified as a not a PRL but classified as a PRL, we can see that

314 hypointensities can manifest around a lesion even when they cannot be rated as a rim.

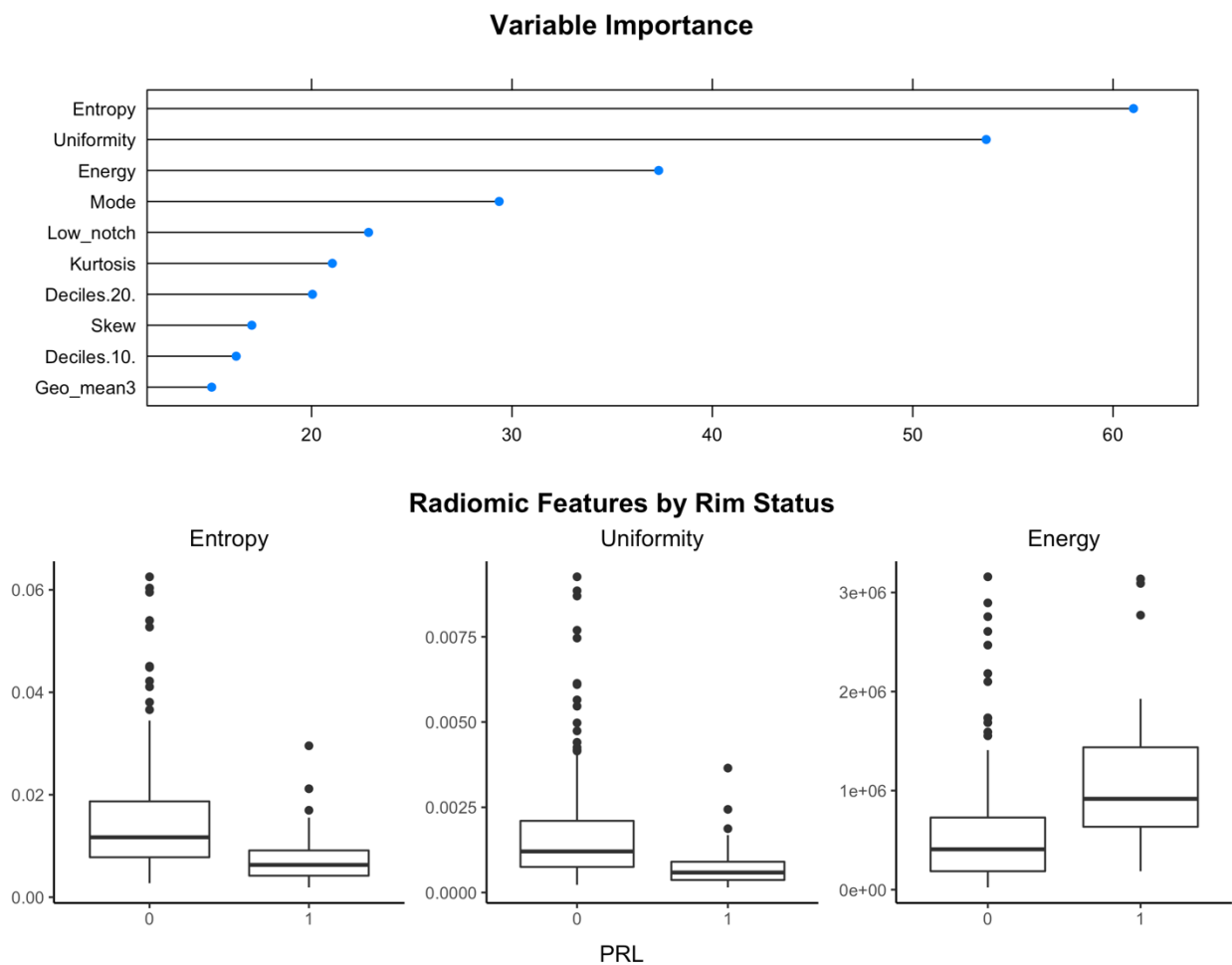
315 Conversely, from subfigure C, which shows a lesion that was identified as a PRL but classified as  
316 not a PRL, we can see that despite the presence of hypointensities that are visible to the eye,  
317 certain PRLs may not display a signal strong enough to be captured by radiomic features.

318

319 The random forest identified uniformity, entropy, and energy as the most important radiomic  
320 features in classifying lesions, which are all radiomic features that aim to describe the diversity  
321 of the data points. (Figure 3). Other radiomic features that were important were mode,  
322 kurtosis, skew, geometric mean, and quantile features. Entropy and uniformity were both  
323 higher in lesions that were not PRL, and energy was higher in lesions that were PRL.

324

325 **Figure 3**



326

327 The variables identified as the most important by our model for determining the presence of  
328 PRLs were entropy, uniformity, and energy. Here, we measure variable importance as the  
329 percent increase in mean squared error for the model with the variable over the model with a  
330 permuted version of that variable, scaled for comparability across variables. Boxplots of  
331 entropy, uniformity, and energy on the lesions from the test set show that PRLs and non-PRLs

332 seem to differ on those measures, supporting the theory that they are important for  
333 distinguishing the two kinds of lesions.

334

335

336 A second expert manually rated the 37 lesions that were misclassified by the model. The rater  
337 deemed that 3 lesions included too much artifact to assess PRL status, and 18 lesions were  
338 confluent lesions. Of the lesions not part of a confluent cluster, 10 were false positive lesions  
339 and 6 were false negative lesions. Of those 10 false positive lesions, 2 of these lesions were  
340 rated as definitely a PRL, 2 were rated as probably a PRL, 4 were rated as probably not a PRL,  
341 and 2 were rated as definitely not a PRL. For the 6 false negative lesions that were not  
342 confluent, 5 were rated as definitely a PRL and 1 was rated as definitely not a PRL.

343

344 As for confluent clusters, 11 were deemed false positives and 7 were false negatives. These  
345 were rated according to the presence of at least one PRL in each confluent cluster. Of the 11  
346 false positive lesions, 4 were rated as definitely not a PRL, 3 were rated as probably a PRL, and 4  
347 were rated as definitely a PRL. Of the 7 false negative lesions, 2 were rated as probably a PRL  
348 and 5 were rated as definitely a PRL. Note that the confluence defined here was as judged by  
349 the manual rater. This differs from but complements the confluence definition employed for  
350 the primary test set analysis, which was the definition based on the automated analysis used to  
351 derive the performance measures reported in Table 4.

352

353

## 354 **Discussion**

355

356 Preliminary studies have shown that the existence of a paramagnetic rim around an MS lesion is  
357 an important biomarker with possible clinical implications, shown to be indicative of chronic  
358 inflammation, associated with heightened disability, and resistant to current disease-modifying  
359 treatments (5). However, paramagnetic rims are time-consuming to identify manually, even by  
360 highly trained experts (17). In this paper, we developed a fully automatic method for the

361 detection of the paramagnetic rim on a 3T MRI using a submillimeter isometric, clinically  
362 feasible, segmented-EPI sequence (17,18). Automation of PRL identification that relies on  
363 objective assessment will aid larger scaled studies assessing this promising imaging biomarker  
364 in MS.

365

366 The proposed method relies on radiomics for automated PRL identification and classification.  
367 Radiomic features have been used previously in other contexts, but none were used specifically  
368 to classify PRLs. The radiomic features that were the most important in this context aimed to  
369 measure the variability of intensity within a lesion (entropy and uniformity) or quantify the  
370 magnitudes of the intensities themselves (energy).

371

372 Both entropy and uniformity are measures based on the probability of observing a particular  
373 intensity within a lesion. Because we did not bin the voxel intensities, this probability of  
374 observing a particular intensity is fairly low, which is reflected in the observed range of  
375 uniformity in this study. Uniformity is a direct measure of homogeneity of the intensities within  
376 a lesion. We expect uniformity to be lower for PRLs due to the presence of both intensities  
377 representing normal appearing tissue and hypointensities from the paramagnetic rim. Lesions  
378 that are not PRLs do not appear with any distinct signature on the phase image, leading to a  
379 higher uniformity.

380

381 Entropy takes the probability of observing a particular intensity within a lesion and transforms it  
382 such that the measure reflects the amount of variation observed. Because of the  
383 aforementioned lack of binning, entropy here more accurately reflects lesion size in that given  
384 our more homogenous set of probabilities, a smaller probability of observing a given intensity  
385 results in a smaller measure of entropy, and larger lesions yield a smaller probability of  
386 observing a given intensity. In this dataset, PRLs tend to have smaller values of entropy,  
387 possibly reflecting a larger size.

388

389 Energy is a measure of the magnitude of intensities within a lesion. Here, PRLs manifest with  
390 higher energy because of the way the phase image was created and the subsequent range of  
391 the intensities. Hypointensities on the phase image used in this study represent more extreme  
392 negative values instead of values closer to 0, with more extreme hypointensities resulting in  
393 more extreme energy values.

394

395 Many of the lesions that the model misclassified were confluent lesions that were labelled as a  
396 single lesion. While the percentages of confluent lesions among correctly classified lesions was  
397 66%, the percentage of confluent lesions among incorrectly classified lesions was 84%,  
398 suggesting that confluence negatively influences the model's ability to classify lesions as PRL or  
399 not. We provide an example of one of these confluent lesions in Figure 1, Subfigure E. In this  
400 lesion, although one of the encompassed lesions contained a clear rim signal, the larger of the  
401 two does not. Because the majority of the voxels included in the confluent lesion belong to the  
402 encompassed one without a rim signal, the first-order radiomic features extracted from this  
403 confluent lesion reflected that signal.

404

405 Artifact made it difficult for a manual rater to rate some of the lesions; our model typically  
406 (perhaps incorrectly) rated these as PRL. Of the "false positive" lesions, as determined by the  
407 initial PRL manual delineations, while half of those were separately rated as definitely or  
408 probably not a PRL, half were rated as definitely or probably a PRL. We also note that for the  
409 false positives, around half of the manual ratings were between 2 and 4 on a 5-point scale  
410 indicating that even for an expert rater, a large portion of these lesions were difficult to classify.  
411 Of the false negative lesions, almost all were rated as definitely a PRL.

412

413 We dilated our lesion segmentation map to increase the likelihood that a rim signal would be  
414 included in a lesion label. Because of this artificial augmentation, periventricular lesions and  
415 lesions closer to the cortex could be difficult to classify due to inclusion of non-lesional phase-  
416 hypointensities in a lesion map, such as ventricles or cortical tissue.

417

418 These issues could be addressed by taking a more nuanced approach to modelling the  
419 probability of having a rim. Here, we treated the identification of PRLs as a binary classification  
420 problem, invoking a random forest to predict if a given lesion was a PRL or not. However, the  
421 identification of PRLs can be difficult because of the myriad of factors that drive the clarity and  
422 strength of a rim signature, some of which are technical and some of which reflect biological  
423 processes. As noted in Figure 1, while some lesions exhibit a rim unequivocally, other lesions  
424 exhibit a more equivocal signature. This renders the task of rating lesions as PRL or not difficult,  
425 both for manual raters and automated classifiers. In fact, previous research has shown that  
426 intra- and interrater reliability for paramagnetic rim evaluation are substantial but not perfect,  
427 with a Cohen  $\kappa$  of 0.77 and 0.71 respectively (17). A future, more nuanced approach could treat  
428 the presence of a rim as a continuous measure instead of a binary classification. This would  
429 likely more accurately reflect underlying biological processes as well, as the amount of iron-  
430 containing phagocytes at the edge of a lesion can vary across lesions (8).

431

432 Limitations:

433 A major limitation to current assessments of paramagnetic rims is that no international  
434 consensus exists on criteria for determining this imaging signature. This limitation may hinder  
435 the application of the proposed methodology to new studies in which differing definitions of  
436 paramagnetic rims may be desired based on local practices. While signal-to-noise ratio is higher  
437 on a 7T MR image, allowing for higher inter- and intra-rater reliability, they remain low across  
438 contrast types on 3T (17). However, our study relies on techniques that perform well on 3T  
439 images, so extensions to 7T would require additional validation.

440

441 In addition, PRLs are a less common type of lesion. In the current study, 13% of the lesions that  
442 were identified had rims. Because they are a rare event, classical machine learning models may  
443 need to be adjusted in order to classify them with appropriate consideration. In the current  
444 study, we employed SMOTE to artificially balance our training data. Other machine learning  
445 methods may benefit more from other solutions.

446

447 **Conclusion**

448

449 This study introduces a fully automated method for the identification and classification of  
450 paramagnetic rim lesions relying solely on 3T MR images, which are commonly available in a  
451 clinical setting. Automation of this process is important for the continued development of the  
452 scientific community's knowledge around these lesions and their implications for disease  
453 burden.

454

455

456 **Funding**

457 Dr. Pascal Sati, Dr. Martina Absinta, and Dr. Daniel S. Reich are supported by the Intramural  
458 Research Program of the National Institute of Neurological Disorders and Stroke, National  
459 Institutes of Health, Bethesda, Maryland, USA. Dr. Martina Absinta is supported by the Conrad  
460 N. Hilton Foundation (grant#17313). Dr. Schindler is supported by the National Center for  
461 Advancing Translational Sciences of the National Institutes of Health under award  
462 number KL2TR001879. Ms. Lou and Dr. Shinohara are supported by awards R01NS112274 and  
463 R01NS060910 from the National Institute of Neurological Disorders and Stroke, and  
464 R01MH112847 from the National Institute of Mental Health. The content is solely the  
465 responsibility of the authors and does not necessarily represent the official views of the  
466 National Institutes of Health.

467

468 **Declarations of interest**

469 None

470

471 **Acknowledgments**

472 We thank the NINDS Neuroimmunology Clinic for recruiting and assessing the patients.

473

474 **References**

- 475 1. Sahraian MA, Radü E-W. MRI Atlas of MS Lesions. Springer Science & Business Media; 2007.  
476 184 p.
- 477 2. Popescu V, Agosta F, Hulst HE, Sluimer IC, Knol DL, Sormani MP, et al. Brain atrophy and  
478 lesion load predict long term disability in multiple sclerosis. *J Neurol Neurosurg Psychiatry*.  
479 2013 Oct 1;84(10):1082–91.
- 480 3. Filippi M, Agosta F. Imaging biomarkers in multiple sclerosis. *J Magn Reson Imaging*.  
481 2010;31(4):770–88.
- 482 4. Sormani MP, Bruzzi P. MRI lesions as a surrogate for relapses in multiple sclerosis: a meta-  
483 analysis of randomised trials. *Lancet Neurol*. 2013 Jul 1;12(7):669–76.
- 484 5. Absinta M, Sati P, Masuzzo F, Nair G, Sethi V, Kolb H, et al. Association of Chronic Active  
485 Multiple Sclerosis Lesions With Disability In Vivo. *JAMA Neurol*. 2019 Dec 1;76(12):1474–83.
- 486 6. Frischer JM, Weigand SD, Guo Y, Kale N, Parisi JE, Pirko I, et al. Clinical and pathological  
487 insights into the dynamic nature of the white matter multiple sclerosis plaque. *Ann Neurol*.  
488 2015;78(5):710–21.
- 489 7. Luchetti S, Fransen NL, van Eden CG, Ramaglia V, Mason M, Huitinga I. Progressive multiple  
490 sclerosis patients show substantial lesion activity that correlates with clinical disease  
491 severity and sex: a retrospective autopsy cohort analysis. *Acta Neuropathol (Berl)*.  
492 2018;135(4):511–28.
- 493 8. Dal-Bianco A, Grabner G, Kronnerwetter C, Weber M, Höftberger R, Berger T, et al. Slow  
494 expansion of multiple sclerosis iron rim lesions: pathology and 7 T magnetic resonance  
495 imaging. *Acta Neuropathol (Berl)*. 2017;133(1):25–42.
- 496 9. Absinta M, Sati P, Schindler M, Leibovitch EC, Ohayon J, Wu T, et al. Persistent 7-tesla phase  
497 rim predicts poor outcome in new multiple sclerosis patient lesions. *J Clin Invest*. 2016 Jul  
498 1;126(7):2597–609.



- 499 10. Kaunzner UW, Kang Y, Zhang S, Morris E, Yao Y, Pandya S, et al. Quantitative susceptibility  
500 mapping identifies inflammation in a subset of chronic multiple sclerosis lesions. *Brain J*  
501 *Neurol.* 2019 01;142(1):133–45.
- 502 11. Chawla S, Kister I, Sinnecker T, Wuerfel J, Brisset J-C, Paul F, et al. Longitudinal study of  
503 multiple sclerosis lesions using ultra-high field (7T) multiparametric MR imaging. *PLOS ONE.*  
504 2018 Sep 13;13(9):e0202918.
- 505 12. Bagnato F, Hametner S, Yao B, van Gelderen P, Merkle H, Cantor FK, et al. Tracking iron in  
506 multiple sclerosis: a combined imaging and histopathological study at 7 Tesla. *Brain J*  
507 *Neurol.* 2011 Dec;134(Pt 12):3602–15.
- 508 13. Absinta M, Sati P, Gaitán MI, Maggi P, Cortese ICM, Filippi M, et al. Seven-tesla phase  
509 imaging of acute multiple sclerosis lesions: A new window into the inflammatory process.  
510 *Ann Neurol.* 2013;74(5):669–78.
- 511 14. Bian W, Harter K, Hammond-Rosenbluth KE, Lupo JM, Xu D, Kelley DA, et al. A serial in vivo  
512 7T magnetic resonance phase imaging study of white matter lesions in multiple sclerosis.  
513 *Mult Scler Houndmills Basingstoke Engl.* 2013 Jan;19(1):69–75.
- 514 15. Mehta V, Pei W, Yang G, Li S, Swamy E, Boster A, et al. Iron Is a Sensitive Biomarker for  
515 Inflammation in Multiple Sclerosis Lesions. *PLOS ONE.* 2013 Mar 14;8(3):e57573.
- 516 16. Hammond KE, Metcalf M, Carvajal L, Okuda DT, Srinivasan R, Vigneron D, et al. Quantitative  
517 in vivo magnetic resonance imaging of multiple sclerosis at 7 Tesla with sensitivity to iron.  
518 *Ann Neurol.* 2008;64(6):707–13.
- 519 17. Absinta M, Sati P, Fechner A, Schindler MK, Nair G, Reich DS. Identification of Chronic Active  
520 Multiple Sclerosis Lesions on 3T MRI. *Am J Neuroradiol.* 2018 Jul;39(7):1233–8.
- 521 18. Sati P, Thomasson DM, Li N, Pham DL, Biassou NM, Reich DS, et al. Rapid, high-resolution,  
522 whole-brain, susceptibility-based MRI of multiple sclerosis. *Mult Scler Houndmills*  
523 *Basingstoke Engl.* 2014 Oct;20(11):1464–70.

- 524 19. Eskreis-Winkler S, Deh K, Gupta A, Liu T, Wisnieff C, Jin M, et al. Multiple sclerosis lesion  
525 geometry in quantitative susceptibility mapping (QSM) and phase imaging. *J Magn Reson*  
526 *Imaging*. 2015;42(1):224–9.
- 527 20. Stüber C, Pitt D, Wang Y. Iron in Multiple Sclerosis and Its Noninvasive Imaging with  
528 Quantitative Susceptibility Mapping. *Int J Mol Sci*. 2016 Jan 14;17(1).
- 529 21. Wisnieff C, Ramanan S, Olesik J, Gauthier S, Wang Y, Pitt D. Quantitative susceptibility  
530 mapping (QSM) of white matter multiple sclerosis lesions: Interpreting positive  
531 susceptibility and the presence of iron. *Magn Reson Med*. 2015 Aug;74(2):564–70.
- 532 22. Rizzo S, Botta F, Raimondi S, Origgi D, Fanciullo C, Morganti AG, et al. Radiomics: the facts  
533 and the challenges of image analysis. *Eur Radiol Exp [Internet]*. 2018 Nov 14 [cited 2020 Jun  
534 30];2. Available from: <https://www.ncbi.nlm.nih.gov/pmc/articles/PMC6234198/>
- 535 23. Coroller TP, Agrawal V, Narayan V, Hou Y, Grossmann P, Lee SW, et al. Radiomic phenotype  
536 features predict pathological response in non-small cell lung cancer. *Radiother Oncol*. 2016  
537 Jun 1;119(3):480–6.
- 538 24. Liu Y, Kim J, Balagurunathan Y, Li Q, Garcia AL, Stringfield O, et al. Radiomic Features Are  
539 Associated With EGFR Mutation Status in Lung Adenocarcinomas. *Clin Lung Cancer*. 2016  
540 Sep 1;17(5):441-448.e6.
- 541 25. Bakas S, Akbari H, Sotiras A, Bilello M, Rozycki M, Kirby JS, et al. Advancing The Cancer  
542 Genome Atlas glioma MRI collections with expert segmentation labels and radiomic  
543 features. *Sci Data*. 2017 Sep 5;4(1):170117.
- 544 26. Li Y, Qian Z, Xu K, Wang K, Fan X, Li S, et al. MRI features predict p53 status in lower-grade  
545 gliomas via a machine-learning approach. *NeuroImage Clin*. 2018 Jan 1;17:306–11.
- 546 27. Yao B, Bagnato F, Matsuura E, Merkle H, van Gelderen P, Cantor FK, et al. Chronic multiple  
547 sclerosis lesions: characterization with high-field-strength MR imaging. *Radiology*. 2012  
548 Jan;262(1):206–15.

- 549 28. Muschelli J, Sweeney E, Lindquist M, Crainiceanu C. fsLR: Connecting the FSL Software with  
550 R. R J. 2015 Jun;7(1):163–75.
- 551 29. Jenkinson M, Beckmann CF, Behrens TEJ, Woolrich MW, Smith SM. FSL. *NeuroImage*. 2012  
552 Aug 15;62(2):782–90.
- 553 30. Smith SM, Jenkinson M, Woolrich MW, Beckmann CF, Behrens TEJ, Johansen-Berg H, et al.  
554 Advances in functional and structural MR image analysis and implementation as FSL.  
555 *NeuroImage*. 2004 Jan 1;23:S208–19.
- 556 31. Yushkevich PA, Piven J, Hazlett HC, Smith RG, Ho S, Gee JC, et al. User-guided 3D active  
557 contour segmentation of anatomical structures: significantly improved efficiency and  
558 reliability. *NeuroImage*. 2006 Jul 1;31(3):1116–28.
- 559 32. Tustison NJ, Avants BB, Cook PA, Zheng Y, Egan A, Yushkevich PA, et al. N4ITK: Improved N3  
560 Bias Correction. *IEEE Trans Med Imaging*. 2010 Jun;29(6):1310–20.
- 561 33. Doshi J, Erus G, Ou Y, Gaonkar B, Davatzikos C. Multi-Atlas Skull-Stripping. *Acad Radiol*. 2013  
562 Dec 1;20(12):1566–76.
- 563 34. Shinohara RT, Sweeney EM, Goldsmith J, Shiee N, Mateen FJ, Calabresi PA, et al. Statistical  
564 normalization techniques for magnetic resonance imaging. *NeuroImage Clin*. 2014 Aug  
565 15;6:9–19.
- 566 35. Valcarcel AM, Linn KA, Vandekar SN, Satterthwaite TD, Muschelli J, Calabresi PA, et al.  
567 MIMoSA: An Automated Method for Inter-Modal Segmentation Analysis of Multiple  
568 Sclerosis Brain Lesions. *J Neuroimaging Off J Am Soc Neuroimaging*. 2018 Jul;28(4):389–98.
- 569 36. Valcarcel AM. mimosa: “MIMoSA”: A Method for Inter-Modal Segmentation Analysis.  
570 [Internet]. 2017. Available from: <https://github.com/avalcarcel9/mimosa>

- 571 37. Valcarcel AM, Muschelli J, Pham DL, Martin ML, Yushkevich P, Brandstadter R, et al. TAPAS:  
572 A Thresholding Approach for Probability Map Automatic Segmentation in Multiple Sclerosis.  
573 *NeuroImage Clin.* 2020 Jan 1;27:102256.
- 574 38. Dworkin JD, Linn KA, Oguz I, Fleishman GM, Bakshi R, Nair G, et al. An Automated Statistical  
575 Technique for Counting Distinct Multiple Sclerosis Lesions. *Am J Neuroradiol.* 2018  
576 Apr;39(4):626–33.
- 577 39. Kolossváry M, Kellermayer M, Merkely B, Maurovich-Horvat P. Cardiac Computed  
578 Tomography Radiomics: A Comprehensive Review on Radiomic Techniques. *J Thorac*  
579 *Imaging.* 2017 Mar 1;33:1.
- 580 40. Kolossváry M, Karády J, Szilveszter B, Kitslaar P, Hoffmann U, Merkely B, et al. Radiomic  
581 Features Are Superior to Conventional Quantitative Computed Tomographic Metrics to  
582 Identify Coronary Plaques With Napkin-Ring Sign. *Circ Cardiovasc Imaging.* 2017 Dec;10(12).
- 583 41. Chawla NV, Bowyer KW, Hall LO, Kegelmeyer WP. SMOTE: Synthetic Minority Over-  
584 sampling Technique. *J Artif Intell Res.* 2002 Jun 1;16:321–57.
- 585 42. Kuhn M. Building Predictive Models in R Using the caret Package. *J Stat Softw.* 2008 Nov  
586 10;28(1):1–26.
- 587 43. Wright MN, Ziegler A. ranger: A Fast Implementation of Random Forests for High  
588 Dimensional Data in C++ and R. *J Stat Softw.* 2017 Mar 31;77(1):1–17.
- 589